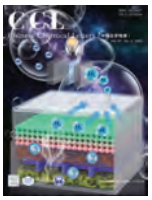
Chinese Chemical Letters 37 (2026) 111611

Contents lists available at ScienceDirect

Chinese Chemical Letters

journal homepage: www.elsevier.com/locate/cclet



Strategies for fabrication and potential applications of conjugated microporous polymer films

Wang Wang[a,1], Miao Feng[a,1], Shuqi Zou[a], Chunxia Chen[a], Jinsong Peng[a], Xiaobai Li[a,*], Shitong Zhang[c,*], Xin Ai[d,*], Hongwei Ma[a,b,*]

[a] Department of Chemistry and Chemical Engineering, College of Chemistry, Chemical Engineering and Resource Utilization, Northeast Forestry University, Harbin 150040, China
[b] Heilongjiang Key Laboratory of Complex Traits and Protein Machines in Organisms, Northeast Forestry University, Harbin 150040, China
[c] State Key Laboratory of Supramolecular Structure and Materials, College of Chemistry, Jilin University, Changchun 130012, China
[d] School of Materials Science and Engineering, Collaborative Innovation Center of Information Technology, Collaborative Innovation Center of Marine Science and Technology, Hainan University, Haikou 570228, China

ARTICLE INFO

Article history:
Received 10 March 2025
Revised 11 July 2025
Accepted 18 July 2025
Available online 18 July 2025

Keywords:
CMP films
Molecular separation
Energy storage
Sensors
Catalysts

ABSTRACT

Conjugated microporous polymers (CMPs) are a class of materials characterized by their rigid π-conjugated network, adjustable microporous structures, and high mechanical strength. Due to these exceptional structural features, CMPs have demonstrated outstanding potential and performance in molecular separation, energy storage, sensors, optoelectronic devices, and catalysts. It has garnered significant attention. However, despite the considerable attention and work paid to synthesizing CMP, the challenges associated with processing it in powders are frequently disregarded. Thus, future advancements must focus on developing strategies to obtain CMPs as film form and how they performed when they are integrated in devices such as batteries, LEDs, supercapacitors, sensors, and solar cells. This paper provides a comprehensive and detailed review of the most recent advances in fabrication strategies and their applications for CMP films as well as the challenges.

© 2026 Published by Elsevier B.V. on behalf of Chinese Chemical Society and Institute of Materia Medica, Chinese Academy of Medical Sciences.

1. Introduction

In the miscellaneous fields of materials science and chemical engineering, the pursuit for state-of-the-art solutions in the potential applications of porous materials has been motivated by their large surface area, inherent porosity, and chemical robustness. These materials provide a promising approach to overcoming challenges across diverse applications, including gas separation [1–4], optoelectronics [5–8], energy storage [9–11], chemical sensing [12–14], biological applications [15–17], and photocatalysis [18–22]. Recent decades have witnessed a concerted effort in developing advanced microporous films.

The progress of film systems, particularly since the late 1960s, has heralded a new era characterized by advances in energy efficiency, operational longevity, environmental sustainability, and compact design. Porous materials have played a pivotal role in this transition by bolstering film performance through precise pore size distribution and heightened porosity. Significant attention has been paid to crystalline porous materials such as zeolites [23,24], polymers of intrinsic microporosity (PIMs) [25,26], metal organic frameworks (MOFs) [27,28], and covalent organic frameworks (COFs) [29–31] for their chemical and physical potential across numerous fields. Nevertheless, their widespread applications are hindered by challenges like structural defects and elevated production costs.

In contrast, traditional amorphous polymers, despite their ease of processing and cost advantages, often lack uniform pore sizes and sufficient porosity. Interest in conjugated microporous polymers (CMPs) has been rekindled due to the innovative solution they provide to surpass the restrictions of traditional porous materials. It was initially just a concept proposed by McKeown and others, until 2007 when Cooper *et al.* synthesized a highly cross-linked microporous network, poly(aryleneethynylene), which marked the birth of the world's first CMP [32,33]. CMPs, characterized by their rigid π-conjugated structures, produce films with uniform pore distribution, extensive surface areas, and exceptional chemical and thermal stability [34]. More importantly, CMP films

* Corresponding authors.
E-mail addresses: lixiaobai2008@126.com (X. Li), stzhang@jluedu.cn (S. Zhang), aixin133@hainanu.edu.cn (X. Ai), mahw@nefu.edu.cn (H. Ma).
[1] These authors contributed equally to this review.

https://doi.org/10.1016/j.cclet.2025.111611
1001-8417/© 2026 Published by Elsevier B.V. on behalf of Chinese Chemical Society and Institute of Materia Medica, Chinese Academy of Medical Sciences.

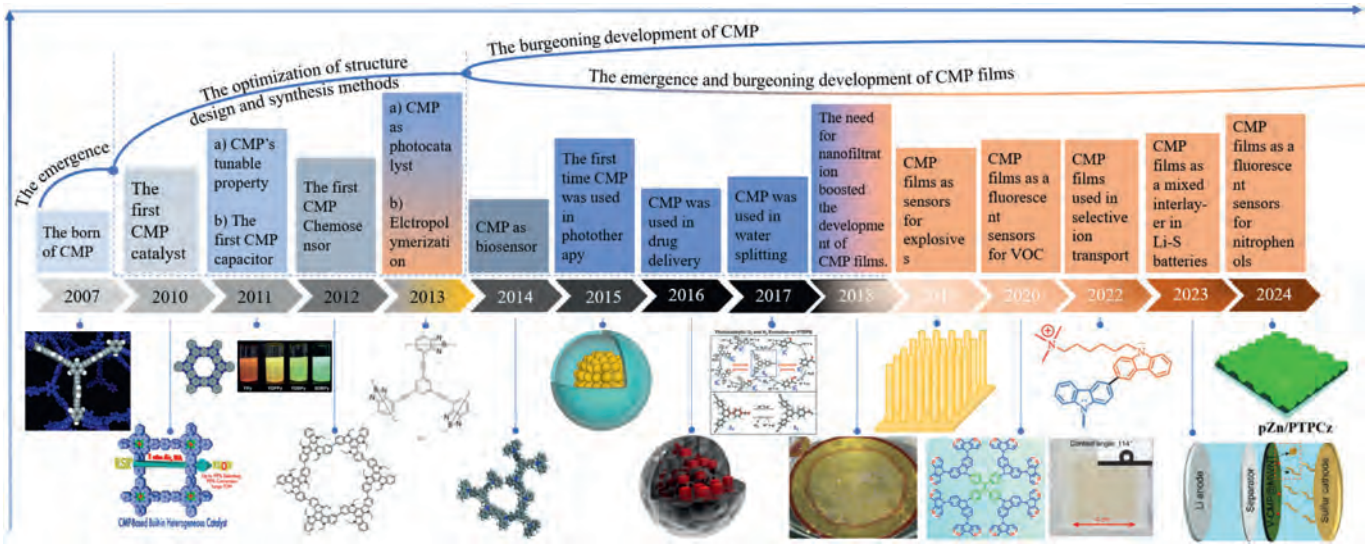


Fig. 1. The big moments of CMP and CMP films development history. The birth of CMP in 2007. Copied with permission [32]. Copyright 2007, Wiley Publishing Group. The first CMP catalyst in 2010. Copied with permission [37]. Copyright 2010, American Chemical Society. The first CMP capacitor in 2011. Copied with permission [9]. Copyright 2011, Wiley Publishing Group. Copied with permission [42]. Copyright 2011, Royal Society of Chemistry. The first CMP chemosensor in 2012. Copied with permission [3]. Copyright 2012, American Chemical Society. The first CMP photocatalyst in 2013. Copied with permission [36]. Copyright 2013, Wiley Publishing Group. Copied with permission [38]. Copyright 2013, Wiley Publishing Group. The first CMP biosensor in 2014. Copied with permission [44]. Copyright 2014, Wiley Publishing Group. The first time CMP used in phototherapy in 2015. Copied with permission [46]. Copyright 2015, Royal Society of Chemistry. The first time CMP used in drug delivery in 2016. Copied with permission [16]. Copyright 2016, American Chemical Society. The first time CMP used in splitting water in 2017. Copied with permission [41]. Copyright 2017, Wiley Publishing Group. The first time CMP used in nanofiltration in 2018. Copied with permission [43]. Copyright 2018, Wiley Publishing Group. CMP films used as sensors for explosives in 2019. Copied with permission [47]. Copyright 2019, Wiley Publishing Group. CMP films used as a fluorescent sensor for VOC detection in 2020. Copied with permission [40]. Copyright 2020, Wiley Publishing Group. CMP films used in selective ion transport in 2022. Copied with permission [48]. Copyright 2022, Wiley Publishing Group. CMP films used in Li-S battery in 2023. Copied with permission [39]. Copyright 2023, Wiley Publishing Group. CMP films used as a fluorescent sensor for nitrophenols detection in 2024. Copied with permission [49]. Copyright 2024, Wiley Publishing Group.

possess significant advantages over their powder form [35]. CMP films combine ease of processing and cost-effectiveness with the unique structural and functional attributes of CMPs. The advancement of CMP films is inherently intertwined with the progress of CMP technology as a whole. The successful applications of CMP across diverse fields lay the foundation for the extensive implementation of CMP films in these domains. We have systematically summarized critical milestones in the development of both CMP and CMP films applications spanning from 2007 to 2024 (Fig. 1) [3,9,16,32,36–49]. As a distinct category in advanced materials, CMP films stand out due to their film-like physical morphologies, amorphous repeating units, horizontally expanded dimensions, and stable covalent cross-linked structures. They demonstrate remarkable flexibility and adaptability across various applications (Fig. 2).

(i) The inherent rigidity of CMP films impedes the free rotation of benzene rings. The quenching of fluorescent groups is thus impeded [50]. In the realms of display technologies and such applications requiring luminescence, CMP films stand out as excellent candidates combined with the ability to introduce various functional groups [12,51].

(ii) The tunable porosity and high surface area of CMP films give birth to their exceptional gas adsorption capacities, which makes them highly selective towards certain molecules in separation technologies [52,53].

(iii) The extensive π-conjugation and adjustable bandgap within CMP films facilitate efficient light capture and energy transfer, which position CMP films as promising materials for photocatalytic applications [32,54,55]. Moreover, CMPs can also serve as precursors to construct carbon superstructures. Apart from their rigid structures, the dual-ion storage mechanism also helps to achieve superior energy storage performance [56,57].

(iv) The coalescence of high specific surface area, micropores, and π-conjugation expose massive active sites in CMP films, which then enhance both the contact with analytes and signal amplification [36,58]. These properties make CMP films naturally sensitive sensors for detecting gas at low concentrations. The intrinsically porous structure of CMP provides enlarged free volume, which is the key to addressing the kinetic constraints of photochromic materials [59].

(v) CMP films exhibit good properties for electrochemical processes. Their rich microporous structure can facilitate rapid electron and ion transport [60,61]. Such structural advantage grants them potential as energy storage materials.

(vi) A combination of microporous structures and optoelectronic properties in CMP films opens up new avenues in light-emitting diodes (LEDs) and solar cells. Their efficient light absorption and emission are crucial [62,63].

From the realms of photoelectricity and catalysis to the intricacies of chemosensors, separation and adsorption mechanisms, energy storage systems, and even ventures into the biological sciences, CMPs have emerged as versatile building blocks with far-reaching applications. However, among the extensive research dedicated to CMPs, a notable void exists, specifically pertaining to CMP films [64]. Recognizing this critical gap in CMP research, this review embarks on a journey to explore and elucidate the latest advancements in CMP film technology [65–68]. This review extends beyond the synthesis method and fabrication strategy to explore the diverse applications of CMP films, including catalysts, optoelectronic devices, sensors, energy storage, and molecular separation. By integrating insights from both fundamental research and practical applications, this review provides a comprehensive understanding of CMP films through retrospective analysis and a prospective outlook.

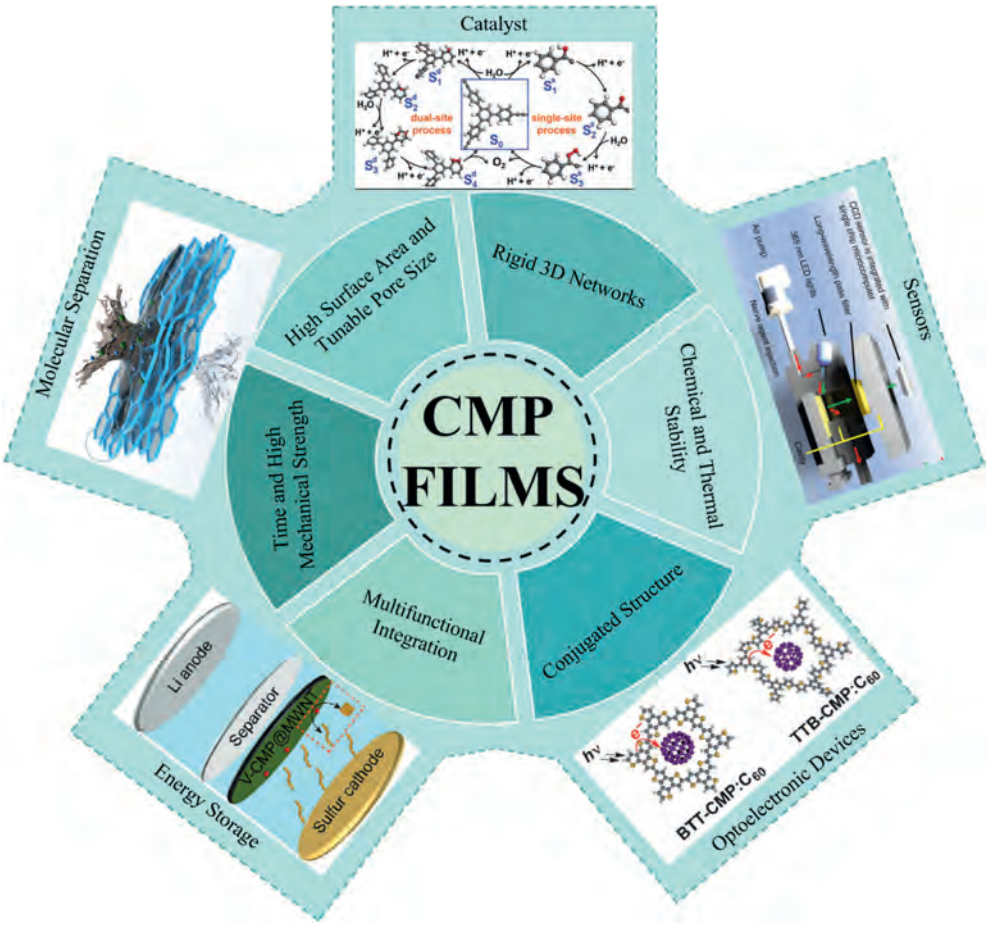


Fig. 2. A graphic illustration of the relationships between application and advantages of CMP films. Reproduced with permission [41]. Copyright 2017, Wiley Publishing Group. Reproduced with permission [45]. Copyright 2022, Nature Publishing Group. Reproduced with permission [143]. Copyright 2015, Wiley Publishing Group. Reproduced with permission [39]. Copyright 2023, Wiley Publishing Group. Reproduced with permission [89]. Copyright 2023, Elsevier.

2. Synthesis methods and fabrication strategies

2.1. Synthesis methods

The development and application of CMPs combine innovative fabrication methods with versatile chemical synthesis. They aimed to tackle their inherent insolubility in common solvents [69]. This characteristic, while enhancing solvent resistance, seriously limits the use of traditional solution-based film preparation techniques. As a response, novel approaches such as surface-confined polymerization, electropolymerization (EP), surface-initiated polymerization, and blending strategies, have been innovated to facilitate the formation of CMP films. In addition to these four major strategies, the synthesis reactions themselves play a crucial role. The commonly used synthesis reactions include phenazine ring fusion reactions [70,71], Yamamoto coupling [72], Sonogashira-Hagihara coupling [73,74], Buchwald-Hartwig coupling [75], Suzuki coupling [37,76,77], oxidative coupling [18], Heck coupling [78], Schiff base reactions [79].

The fabrication strategies of CMP films can be found in Text S1 (Supporting information).

3. Advanced applications of CMP films

The allure of CMP films lies in their adjustable porous structure and specific functionalities that can be adjusted by modifying monomers or post-functionalization techniques. Moreover, these CMP films, with their π-conjugation and rigid network structure, show exceptional chemical and thermal stability. The versatility of these features makes them suitable for various uses, including separation, energy storage, sensors and optoelectronic devices, and catalyst.

3.1. Molecular separation

3.1.1. Organic solvent nanofiltration (OSN)

CMP films are inherently insoluble in organic solvents, which has led to the prevalent method of fabricating them from organic solutions [80]. In 2014, Lindeman and colleagues devised a CMP-MOF system utilizing linkers with dual azide side groups [81]. After constructing the CMP film of 8 nm thickness, it was immersed in an EDTA solution to dissolve the MOF substrate (Fig. S4a in Supporting information) to reveal the gas separation capabilities of the film. Four distinct batches of PAN/PDMS/CMP TFC films were synthesized, which have unique gas permeation characteristics that facilitate selective gas separation. However, a significant hurdle in producing CMP films *via* organic solvents is the costly purification of these solvents. Liang *et al.* implemented to yield a 42 nm thick CMP film on polyacrylonitrile substrates *via* surface-initiated polymerization method [52]. It boasted impressive nanofiltration capabilities for permeance of 32 L m^{-2} h^{-1} bar^{-1} for hexane and 22 L m^{-2} h^{-1} bar^{-1} for methanol. Moreover, *p*-CMP, *m*-CMP, and *o*-CMP exhibit much better rejection behavior surpassing those of analogous materials (Fig. S4b in Supporting information). Moreover, the idea that porosity and pore size of CMPs can be precisely controlled by incorporating various functional groups was verified

by the introduction of hydroxyl, acetyl, benzoyl, and adamantane formyl groups on *p*-CMP [82]. Surprisingly, such enhancement in dye rejection overcame the impossibility of adjusting pore size and specific functions of CMP films at a molecular aspect [83]. A gradual decrease was observed in the BET surface areas after being modified with hydroxyl, acetyl, benzoyl, and adamantane formyl groups. A significant and progressive increase was also found in dye rejection (Fig. S4c in Supporting information). Building on the concept of meticulous pore size regulation *via* integrated functional groups (Fig. S4d in Supporting information), Tang and his team made a step forward. They proposed a novel method for fine-tuning CMP film pore sizes at the angstrom scale [84]. By oxidizing the thiophene units, the two center pore size distributions of the TTB-CMP films reduced 0.26 nm and 0.30 nm. This method offered a technique for directly manipulating pore sizes at the angstrom level with maintained permeance efficiency [85–88].

Fabricating freestanding CMP films with accessible porosity is a huge challenge. In 2023, Hardian *et al*., used a two-step solvothermal method, synthesized three types of CMP films, B-BOP, TPPy-BOP, and TPB-BOP with pore size of 1.4, 1.6, and 2.8 nm [89]. A benzimidazole catalyst was introduced to avoid premature polymerization in the solution. The thickness of B-BOP, TPPy-BOP, and TPB-BOP films were 1.47 ± 0.04, 1.46 ± 0.05, and 2.70 ± 0.07 μm, respectively. They synthesized a new material using 0.025 mmol of DAHQ and a benzimidazole catalyst in an NMP/mesitylene solvent. By employing a process of controlled heating followed by vacuum annealing, they achieved a high-performance oxazole product (Fig. S4e in Supporting information). Thinner films are generally favorable for nanofiltration. To test the function stability of all BOP films, all the films were set in the continuous filtration for 120 h. Moreover, they compared the structures and the corresponding properties of CMP films with and without the introduction of F atoms. It was found that they had highly similar structures except for the fluorine substitution at the triphenylbenzene node. However, TPB-F-BOP exhibited higher molecular weight cut-off (MWCO) and flux value. This was attributed to the F atoms regulating the conjugated framework towards a more regular direction. It also proved that introducing halogen atoms to enhance covalent framework structural order was an efficient solution to increase the uniformity of surface area and intensify its permeability performance. Their amorphous nature provided evidence against the conventional mechanism that solute passes through ordered channels within material frameworks.

Su *et al*. reported a solvent-resistant C–C bonded CMP (CCMP@PTFE) film by constructing channels in polytetrafluoroethylene (PTFE) ultrafiltration films through space-confined polymerization (Fig. S4f in Supporting information) [90]. The CCMP@PTFE films demonstrated excellent permeability of 80.7 L m^{-2} h^{-1} bar^{-1} for small dye molecules like ethanol and ultrafast pure solvent permeance of 335.1 L m^{-2} h^{-1} bar^{-1} for methanol. Moreover, these films exhibited outstanding long-term stability and remarkable solvent resistance.

3.1.2. Gas separation

The rigid pore structure of CMPs is the foundation of gas separation. It ensures the fixed and stable pore size and distribution during gas separation processes. Unlike conventional flexible polymers, they are prone to swelling and deformation and lack durability. Conventional polymeric films prevail in the commercial market due to their affordability, stability, and processing simplicity. However, they consistently confront the difficulty of harmonizing permeability and selectivity [91].

Zhang *et al*. developed fourteen films, with thicknesses of 1–2 μm, employing Softness Adjustment of Rigid Network (SAR) strategies alongside EP (Figs. S5a and b in Supporting information). Surprisingly, this CMP film, P33DT-ThC4, exhibited exceptional H_2/CO_2 selectivity level up to 50 with H_2 permeability of 626 Barrers [92]. These two remarkable advantages placed it at the leading edge of contemporary pure organic polymer films (Fig. S5c in Supporting information). Additionally, it presented remarkable resistance under acidic and thermal conditions and maintained its separation efficiency in the presence of aggressive gases such as hydrogen sulfide (H_2S) and at temperatures reaching 120 °C (Fig. S5d in Supporting information). The theoretical calculation by semiempirical formula suggested the pore sizes centered at 0.35 and 0.66 nm. This calculated outcome fell between 0.28 nm and 0.68 nm, examined by positronium annihilation lifetime spectroscopy (PALS) measurements and ensured both selectivity for H_2/CO_2 and permeability for H_2. The smaller pore size that closely matched the kinetic diameter of CO_2 could enhance the film's H_2/CO_2 selectivity. The free-standing CMP films reported by Lindeman *et al*. in the subsequent year demonstrated significantly lower H_2 permeability. It fell below the Robertson upper limit at 4 Barrers [81]. This comparison highlighted the superior gas separation efficiency of the P33DT-ThC4 film.

3.1.3. Ion sieving

Compared to separation processes such as nanofiltration and solvent extraction, the primary challenge for ion sieving resides in the uniformity of particle sizes. Zhou *et al*. used 1,3,5-tris(*N*-carbazolyl)benzene (TCB) as monomer and developed a CMP film with a high BET surface area of 809 m^2/g for ion separation [93]. To enhance CMP film's mechanical strength, carbon nanotubes (CNTs) were introduced during the preparation. EP by CV scans within the range from −0.8 V to 1.23 V enabled controlled film thickness (Figs. S6a and b in Supporting information). The meticulously optimized CMP@100–20c film was developed at a scanning rate of 100 mV/s over 20 cycles. It exhibited precise thickness management and a granular surface texture. This film showed a pore-size distribution centered at 8.4 Å (Fig. S6c in Supporting information). However, due to the distortion and extension during the separation process, ions with little larger diameters could still travel through the films. Moreover, it also boasted a high BET surface area of 809 m^2/g. Transparently, ion sieving requires extremely precise pore sizes and a high-level of pore size uniformity. Unlike organic molecular nanofiltration and gas separation, they do not have such strict demand on porosities and pore size distributions [94,95]. They also looked into how the increasing probe diameters (4, 6, 8 Å) affected the film's porosity. It turned out that smaller probes tended to show high porosity with those interconnected voids, while larger probes led to the decreased interconnectivity. This film exhibited hydrophilic properties with a water contact angle of 77.9° ± 4.3°. Sustained filtration experiments on CMP@100–20c showed enduring effectiveness and pressure-driven assessments highlighted a pronounced rejection curve. The selectivity of the CMP@100–20c film achieved about 140 for Na^+/RhB and 135.9 ± 4.1 for Mg^{2+}/RhB. Both results surpassed the previously documented selectivity of 120 for salt/dye combinations (Fig. S6d in Supporting information).

However, the fragility of CMP films results in their reduced mechanical properties. Therefore, there is a critical need for the development of flexible CMP films that have a well-structured pore network and are chemically stable to meet the requirements for ion sieving. The ion-sieving efficiency of CMP films developed by Zhou *et al*. in Fig. S6e (Supporting information) was evaluated through concentration-driven and electrically-driven permeation assays [96]. These CMP films of 40 nm thickness demonstrated exceptional selectivity towards specific ions, as indicated by an H^+/Mg^{2+} selectivity ratio of 9.3, which was considerably higher than the 2.6 ratio seen in Nafion 117. When a diffusion agent like $MgCl_2$ was introduced into the system, it would lead to the decrease of ion conductivity of the CMP films. It was mainly due to

the positive-charged groups impeding the permeation of cations. In concentration-driven tests, the transport of Na_2SO_4 through the CMP films was remarkably more efficient than that of NaCl. This observation was attributed to the interaction between the divalent anions (SO_4^{2-}) and the film's positively charged groups. It facilitated the transport of the divalent anion salt (Na_2SO_4). This phenomenon clarified that ion transport across CMP films is controlled dually by size and charge. Moreover, the different rates at which H^+, K^+, Na^+, and Li^+ ions permeate during concentration-driven tests highlighted the films' specific selectivity, which is determined by the size and charge of the ions (Fig. S6f in Supporting information). This thorough examination emphasizes the intricate and exceptional ion-separating characteristics of CMP films. Both Zhang *et al*. and Zhou *et al*. employed EP to produce CMP films to prevent additional processing and undesired thickness increments that may hinder ion transport efficiency. Films with increased thickness exhibit higher resistance to the decrease in potential during ion transport, which can negatively impact transmission efficiency or impede it.

The advancement of artificial systems for effective ion transportation has a profound impact on energy storage, photo-driven ion separation, and water treatment. Nevertheless, the task of generating active ion transport in nanoporous materials composed entirely of solid-state components continues to be a significant obstacle [97]. Yang *et al*. addressed this challenge by fabricating a Janus microporous film. It was composed of reduced graphene oxide (rGO) and CMP [95]. Inspired by photovoltaic devices' principles of p-n junctions, light was initially converted into separated charges to generate a transmembrane potential. This potential subsequently drove ions moving in a certain direction and achieved controllable photo-driven ion transport. The Janus microporous film was fabricated *via* sequential electrochemical polymerization of thiophene-containing CMPs (TTB-CMP) (Fig. S6g in Supporting information). The pore size of the TTB-CMP predominantly fell between 1.47 nm and 1.73 nm. To achieve inherent self-supporting and flexible properties, rGO/CMP hybrid films were processed with thermal annealing. The transmembrane potential was directly proportional to light intensity, which indicated that increasing light intensity can promote ion transport. Thicker rGO layers have higher ion conductivity. However, increasing the thickness of the rGO layer would result in a decrease in current density. Furthermore, the ion transport in the rGO/CMP Janus film was highly dependent on the hydrated ion radius.

3.2. Energy storage

3.2.1. Battery

Lithium-sulfur (Li-S) batteries are one of the most promising contenders for next-generation energy storage systems due to their high discharge capacity, low cost [98,99]. However, their applications face several challenges. Majority of the polysulfides suffer from the shuttle effect and such phenomenon can lead to the slow reaction kinetics, capacity decay, and poor cycling stability [100–102]. To address these issues, CMPs have been used as suitable sulfur hosts in the batteries. Jia *et al*. electrochemically grew a polymer of 5,5′-di(9*H*-carbazol-9-yl)-2,2′-bipyridine (DCBPY) on the surface of a conductive multi-walled carbon nanotube (MWNT) film to form V-CMP@MWNT (Fig. 3a) [39]. However, the thermal stability of V-CMP@MWNT was relatively poor. It begins to decompose at 200 °C. As a sulfur host, it provided a sulfur loading of 12.2 mg/cm^2. The V-CMP@MWNT interlayer exhibits the best cycling stability compared to the control group. It still achieved 616 mAh/g after 1000 cycles under 0.5 C (1 C = 1675 mAh/g). Moreover, it had a rate capability of 804 mAh/g at 10 C. Liu *et al*. synthesized a ST-CMP film by polymerizing squaric acid and 1,3,5-tris(4-aminophenyl)benzene onto CNTs through *in situ* template-oriented polymerizations to form a ST-CMP film (Fig. 3b) [60]. The S/ST-CMP@CNT film achieved a remarkable initial specific capacity of 1307 mAh/g at 0.2 C and a capacity loss rate of only 0.047 % per cycle after 500 cycles at 1 C. Guo *et al*. successfully synthesized ultrathin, continuous CMP films through EP, which demonstrated outstanding conductivity and an ability to mitigate polysulfide shuttling (Fig. 3c) [103]. Their Li-S full battery showcased a remarkable capacity of 10 mAh/cm^2 at a sulfur loading of 11.2 mg/cm^2. This CMP film effectively reduced the shuttle effect of polysulfides while enhancing lithium-ion transport. Although the film does not completely prevent capacity degradation, particularly during the initial 100 cycles, substantial performance improvements were observed. The UCCM/PP cells exhibited no significant polarization effects as the discharge rate increased from 0.1 C to 1 C. When it was raised to 3 C, the reversible capacity of the system reached 680 mAh/g. It surpassed the performance of both CNT/PP and PP cells under comparable circumstances. The UCCM@C/PP cells exhibited consistent rate capability at 1 C and sustained a stable capacity of around 680 mAh/g over 300 cycles. In addition, its Coulombic efficiency neared 100 %. These results offer vital insights and direction for developing advanced Li-S batteries.

Lithium metal anodes are famous for their high specific capacity, low redox potential, and high energy density [104]. Especially when it comes to energy and power densities, lithium batteries outstrip those of lithium-ion batteries. However, the safety of lithium metal anodes continues to be a major matter of concern. Furthermore, they perform less remarkable in terms of cycle life. In 2021, Zhang *et al*. utilized CMP nanosheets to form a dense film on the lithium anode to tackle this issue (Fig. 3d) [105]. The CMP layer facilitated Li stripping/plating and significantly reduced polarization; a benefit attributed to the inherent sub-nanometer pores (5–6 Å in diameter) in the CMP nanosheets. Furthermore, batteries equipped with CMP-Li anodes demonstrated exceptional long-term stability. It stayed chemically and morphologically stable over 2550 h under current densities of 20 mA/cm^2. Such remarkable electrochemical properties of the CMP film layer can be ascribed to its nanoscale channels, which realize the uniform dispersion of ions throughout the battery and hinder harmful interactions at electrolyte-electrode interface.

To address the challenges of low operating voltage, limited capacity, and low energy density faced by symmetric all-organic batteries (SAOBs) [106,107], Yu *et al*. designed and synthesized two CMPs containing p-n bipolar redox-active centers [108]. The C=N bond contained in bithiazole moiety in TPSZ granted it a much narrower band gap compared with TPDS and such band gap facilitated electron transport and improved electrochemical stability. When TPSZ-CMP was served as the cathode material, it overcame the problem of low operating voltage with a value of 2.7 V and when it was used as a negative electrode it showed a potential of 0.6 V. Such cell could provide a superior discharge capacity of 120 mAh/g at current densities of 100 mA/g. Moreover, it was tested after 100 cycles and exhibited a terrific cycling stability with 85 % capacity.

In 2024, Hu *et al*. made a huge breakthrough in integrating CMP as cathodes for zinc-organic batteries [109]. This design integrates bipolar CMPs with reduced graphene oxide (rGO) through intermolecular interactions to construct hybrid materials featuring dual redox-active centers. This innovative architecture enables synergistic anionic/cationic co-storage while maintaining over 90 % capacity retention after 25,000 cycles. Such improvement surpassed the most reported research [110–114].

3.2.2. Supercapacitor

Supercapacitors are distinguished by their strong stability under high current densities. This stability is given by the rigid cross-linked network structure and abundant pores within CMP. It can

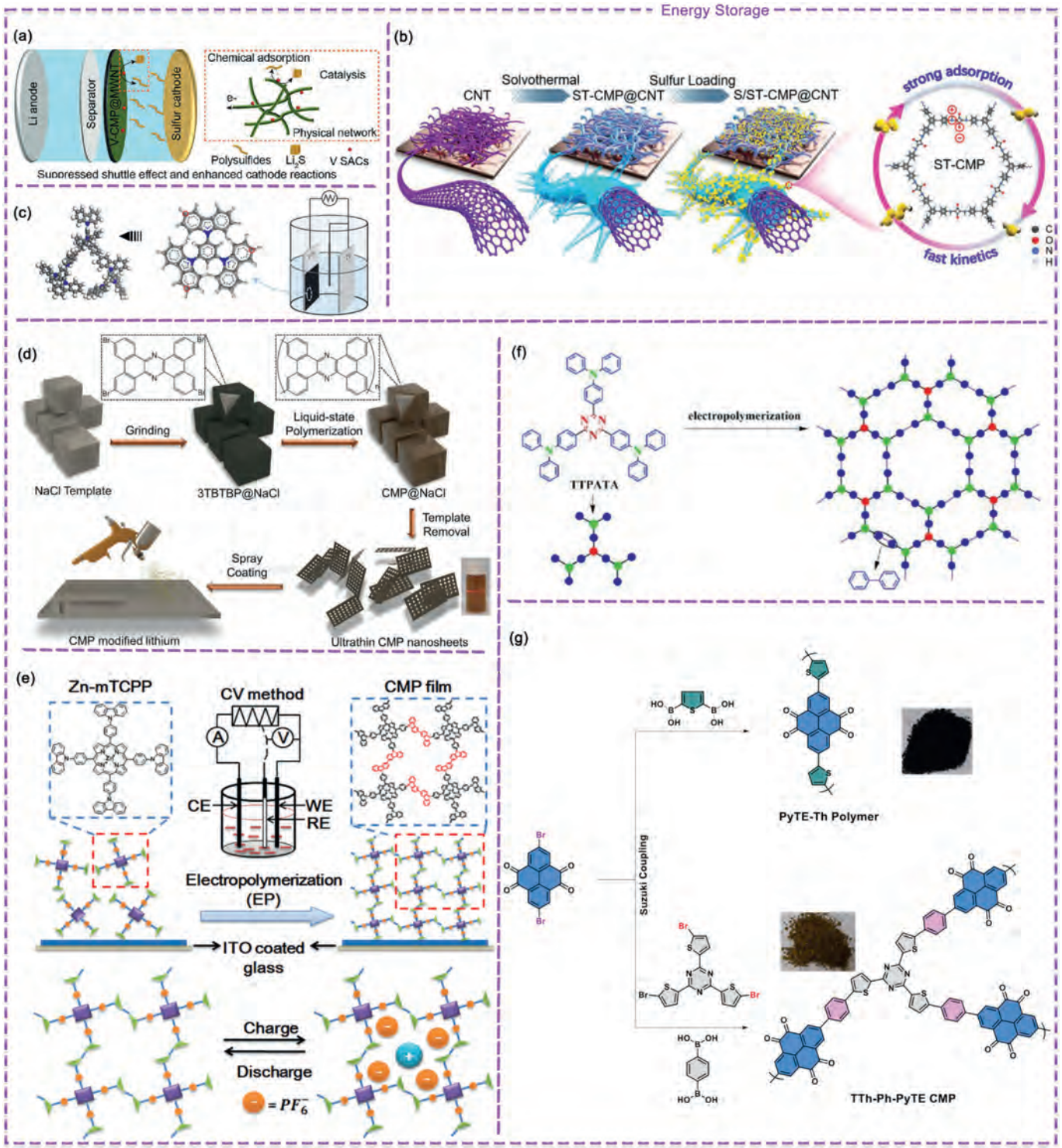


Fig. 3. (a) Graphic explanation of the suppressed shuttle effect and enhanced cathode reactions. Reproduced with permission [39]. Copyright 2023, Wiley Publishing Group. (b) The fabrication of S/ST-CMP@CNT film. Copied with permission [60]. Copyright 2021, Wiley Publishing Group. (c) From left to right: CMP film's pore structure, the TCB monomer structure, highlighting the carbon atoms (marked with a red circle) as active polymerization sites, and a three-electrode electrochemical system. Reproduced with permission [103]. Copyright 2020, Elsevier. (d) The synthesis of CMP-Li film. Copied with permission [105]. Copyright 2021, Wiley Publishing Group. (e) Illustration of the EP technique used to create Zn-porphyrin-based CMP films. Copied with permission [108]. Copyright 2024, Elsevier. (f) The EP process of TTPATA with a possible idealized polymer structure. Copied with permission [119]. Copyright 2019, Royal Society of Chemistry. (g) Schematic illustration of the synthesis of TTh-pH-PyTE and PyTE-Th. Copied with permission [123]. Copyright 2025, Elsevier.

facilitate rapid electron transfer. In addition, a higher BET surface area is generally associated with greater capacitance. Zhang *et al.* made a CMP film supercapacitor. It achieved a BET of 1450 m^2/g and a specific capacitance of 142 F/g (Fig. 3e) [108]. Initial anodic scanning revealed a peak between 0.6 V and 0.85 V. This was because of the oxidation of zinc-porphyrin cores. The redox peak of dimeric carbazole indicated the absence of further oligomer formation and clear structure [115,116]. When the thickness of CMP films surpassed 60 nm, the films detached and were obtained as free-standing films spontaneously. Furthermore, the doping of CMP films is crucial for the superior performance of highly doped supercapacitors [117]. It can facilitate charging and discharging during the doping/de-doping processes to maintain electrical neutrality. The doping process was immersing CMP films in a CH_2Cl_2 solution containing 0.1 mol/L Bu_4NPF_6 at an anodic potential of 1.4 V for 180 s. The doped CMP film had a broad tail band of bis(carbazole) cations in the UV–vis spectrum, with a doping level of 30%. This data correlates to high conductivity and excellent specific capacitance. The film thickness of the electrode is pivotal in charge transfer resistance during charge and discharge processes [118]. However, calculations based on high-frequency semicircles indicated that film thickness ceased to be the primary factor affecting ion transfer for thicknesses in the tens of nanometers. Therefore, selecting films of moderate thickness within this range can optimize coverage and prevent detachment due to excessive scanning.

Dai *et al.* reported a pTTPATA CMP based on triphenylamine-triazine (Fig. 3f) [119]. It was notable for its voltage-dependent color responses. When pTTPATA was served as the negative electrode, its color transitioned from light red to dark red and then to blue during the charging process. When discharging, it shifted from dark red to light red, eventually becoming pale yellow. The color changes observed in the pTTPATA polymer were mainly caused by the presence of triphenylamine radical cations. These color changes signal the activation of structural resonance in polymers' oxidized state, which also help to explain their high specific and volumetric capacities of up to 81 mAh/g.

The CMP-MoS_2-CMP sandwich structure provides abundant active sites and ion transport pathways by its solution-processable nanosheet assembly technique. Yuan *et al.* synthesized MoS_2-templated CMP (MCMP) nanosheets by cultivating N-rich CMPs on MoS_2 templates functionalized with 4-iodophenyl groups [120]. MCMP nanosheets exhibited a higher diffusion-limited current, which ultimately achieved a high capacitance of 344 F/g at a current density of 0.2 A/g. It was because of the effective charge storage provided by interlayer and intralayer bilayers or pseudocapacitance around Mo centers. With the burgeoning demand for flexibility, flexible solid-state supercapacitors (FSSCs) have obtained widespread attention as wearable devices. To address the issue of low energy density, Liao *et al.* designed two porous composite films used for the electrode with BET of 982 m^2/g [121]. The sandwich structure of CMPs/graphene is a classic configuration to satisfy the flexibility need. However, it begins to decompose when it reaches 300 °C. The PTPAH@rGO CMP film electrode exhibited a specific capacitance of 545 F/g and 450 F/g at current densities of 1 A/g and 10 A/g respectively.

Kuo *et al.* reported two CMPs, TBN-TPE and TBN-TP, with BET of 126 and 230 m^2/g and Td5 of 372 and 332 °C [122]. Compared to the monomer of TBN-TPE, the tris(4-aminophenyl)amine precursor in TBN-TPA enhances conductivity tough the stacking of benzene rings, while its high porosity facilitates ion diffusion. The specific capacitance of TBN-TPA is nearly twice that of TBN-TPE, which is not only attributed to its larger surface area but also to the improved electron dispersion enabled by the benzene ring stacking in the TPA units. Although the charge transfer resistance of TBN-TPA is six times higher than that of TBN-TPE, its knee frequency is nearly 100 times greater, indicating superior rate performance at high current densities. In 2025, the same research group successfully synthesized two CMPs, TTh-pH-PyTE and PyTE-Th polymer, through Suzuki coupling reactions (Fig. 3g) [123]. TTh-pH-PyTE CMP exhibited a BET surface area of 55 m^2/g, a pore volume of 0.15 cm^3/g, a Td5 of 445 °C, and a char yield of 67 wt%. In a three-electrode system, TTh-pH-PyTE CMP demonstrated a high specific capacitance of 1041 F/g at 1 A/g, with an energy density twice that of PyTE-Th. In symmetric supercapacitor testing, TTh-pH-PyTE CMP achieved a specific capacitance of 242 F/g at 1 A/g and retained 93% of its capacity after 5000 cycles. The performance advantages are primarily attributed to N and S doping enhancing charge delocalization, a porous structure facilitating ion transport, and a hydrophilic surface with a contact angle of 23.2° improving electrolyte wettability. Additionally, the synergistic redox reactions of TTh^{2-} and $PyTE^{4-}$ also contributed to an overall enhancement in capacitance. Apart from doping, introducing sulfone groups can also enhance the wettability [124].

3.3. Sensors

3.3.1. Electrochemical sensors

CMP films are promising candidates for electrochemical sensor enhancement. Their excellent conductivity can boost electron transfer. Moreover, large specific surface area can offer more active sites. Scherf and colleagues synthesized TPTCz CMP by reacting tetra(4-bromophenyl)methane, carbazole, and other reagents in 1,2-dichlorobenzene at 180 °C for three days (Fig. S7a in Supporting information) [125]. The obtained TPTCz CMP boasted a BET of 1331 m^2/g. After purification, TPTCz was used to fabricate PTPTCz CMP films. GC electrodes modified with PTPTCz CMP films demonstrated remarkable sensitivity towards nitroaromatic compounds at 0.1 μmol/L concentration. It displayed distinctive reduction peaks for different explosives (Fig. S7b in Supporting information). Even at ppb level concentrations, PTPTCz-modified GC electrodes demonstrated excellent selectivity and sensitivity in an aqueous environment. Based on their experiment, Bai *et al.* explored the growth of CMP films by chronoamperometry and CV [126]. These methods' scanning rates and deposition times varied and resulted in polymers PBT CMP (polymers for 3,3′-bithiophene), PTTB CMP (polymers for 1,3,5-tri-(thiophen-2-yl)benzene), and PTTPA CMP (polymers for tris(4-(thiophen-2-yl)phenyl)amine). The PTTB-coated electrodes showed better detection of metronidazole compared to the unmodified electrodes. Although the conductivity decreased in some cases due to the increased film thickness, the conductivity could be increased by the efficient charge transfer promoted by the thiophene-based polymer structure.

In addition to liquid detection, gas detection often demands higher sensitivity. In 2024, Song developed two CMP films containing pyrimidine (Py-COP) and boron β-diketone (BF-COP) to enhance the sensitivity and humidity resistance of organic semiconductor gas sensors (Fig. S7c in Supporting information) [127]. It is worth noting that BF-COP demonstrated an outstanding sensing response to NH_3 concentrations as low as 40 ppm at room temperature, which achieved a response value exceeding 1500 (R_a/R_g) and stood out as one of the highest among original COPs categorized as n-type sensing materials (Fig. S7d in Supporting information).

The organic semiconductor (OSC) gas sensor developed by Gou *et al.* exhibits remarkable mechanical flexibility and has attracted considerable interest for potential applications in commercial and wearable technologies [128]. This innovation addresses a common problem in traditional wearable devices, namely that the sensing layer cracks easily when subjected to bending. Concurrently, Song *et al.* presented a doped CMP film that exhibited high bending durability [129]. Based on this crucial progress, they built a low-power, flexible, and wearable sensor for dimethyl methylphos-

phonate (Fig. S7e in Supporting information). The proximity of the gold's Fermi level to the HOMO level of PQST12 not only reduces power consumption but also facilitates rapid carrier transport. This device only had a mere 28 nW of power consumption when being operated at 1 mV. The sensing detection range started from 0.005 ppm to 100 ppm with three operation stages, which is lower than 0.03 ppm, from 0.03 ppm to 1.2 ppm, and higher than 1.2 ppm (Fig. S7f in Supporting information). However, all wearable devices encounter cracking issues. To address these issues, Cho *et al*. found that inserting atom-level thin intermediate layers, such as graphene, molybdenum disulfide, and hexagonal boron nitride, could increase electrical resistance under strain [130].

3.3.2. Fluorescence sensors

Fluorescence detection stands out for its affordability, real-time monitoring capabilities, simplicity, portability, and ease of integration into devices, which receives increasing public interest [131–134]. In 2016, Räupke *et al*. developed CMP films from PSpCz to detect nitroaromatic compounds with its 1300 m^2/g surface area (Fig. 4a) [135]. They synthesized PSpCz CMP films *via* EP on ITO electrodes and compared it to thermally evaporated SpCz monomer samples. The sensing device setup is schematically shown in Fig. 4b. Fig. 4c demonstrates PSpCz's high sensitivity with significant photoluminescence quenching at low TNT concentrations (5 ppb). Aggregation-caused quenching (ACQ) can greatly reduce the fluorescence intensity of the materials [136]. Such phenomenon arose from π-π stacking in the aggregate state. In contrast, aggregation-induced emission (AIE) can enhance a fluorophore's emission in aggregated states. This phenomenon was initially identified by Tang and his team [137]. Our team in 2020 constructed a high-luminescence CMP film using a novel dendrimer, TPETCz, as reported in Fig. 4d [40]. Such CMP film's BET surface area reached 1042.5 m^2/g. This CMP film remarkably boosted fluorescence when exposed to electron-rich volatile organic compounds (VOCs) and it exhibited an obvious fluorescence quenching when exposed to electron-deficient VOCs. Such prominent sensitivity to VOC vapors primarily results from AIE effect and boosting excited electron transfer by higher LUMO of VOCs stimulants. The CMP film's response to VOCs shows a broad linear range. In 2022, our team synthesized two molecules TCz-CMP and TCzP-CMP based on hybrid local and charge transfer (HLCT) precursors [45]. TCzP-CMP's pore size distribution is much centered than that of TCP-CMP. Although the average pore size of TCzP-CMP is smaller than that of TCz-CMP, it accidentally made TCzP-CMP better for DCP diffusion. Either of them boasted an excellent on/off ratio on acid substrates of the HLCT character. We also devised a portable fluorescence detection system (Fig. 4e) integrating an air pump, TCzP-CMP film, a 365 nm LED, an optical recognition system, and a Bluetooth transceiver, within a sealed chamber. This system demonstrated enhanced sensitivity to acid-containing DCP vapors, with limit of detections of 0.032 ppt for TCz-CMP and 0.14 ppt for TCzP-CMP.

3.4. Optoelectronic devices

3.4.1. Light-emitting diodes

CMP can effectively capture light energy and convert and transfer the energy to the electrical device in need. Such advantages have enabled CMP to quickly keep up with the development of organic electronics and gain widespread attention. In a study carried out by Gu *et al*., CMP films were prepared *via* electropolymerization [38]. These CMP films were employed as anode interlayers in polymer light-emitting diodes (PLEDs). To achieve high-performance devices, the PLEDs were applied with poly[2-(4-(3′,7′-dimethyloctyloxy)-phenyl)-*p*-phenylenevinylene] (P-PPV) to serve as the emissive layer. Comparative experiments were conducted with PLEDs using PEDOT:PSS as the anode interlayer and it resulted in a 51 % enhancement in luminous efficiency for $LiClO_4$-doped CMP devices (Fig. S8a in Supporting information). It reached a peak brightness of 33,000 cd/m^2 and a luminous efficiency of 20.7 cd/A as an electrode interlayer. Such enhancement was due to the elevated work function and enhanced conductivity that facilitated the hole injection and showed its great potential in organic electronics [138,139]. Compared to PEDOT:PSS, doped CMP devices exhibited a 37 % efficiency improvement as the anode interlayer. This research indicated doped CMP films as a good option as anode interlayers in boosting LED device performance in luminous efficiency.

Liang *et al*. utilized two different electrolyte solutions for TCTA and OCBzC in their study to synthesized TCTA OEP and OCBzC OEP films by organic EP process (OEP) (Fig. S8b in Supporting information) [140]. Devices utilizing either ITO/TCTA OEP film (18 nm) or not/OCBzC OEP film (80 nm)/TPBi (35 nm)/CsF (1 nm)/Al (100 nm) displayed similar electroluminescent characteristics. Compared with naked ITO, introducing TCTA OEP film as the hole transport layer (HTL) brought a significant improvement. The luminance efficiency was 2.3 times larger and power efficiency increased 1.6 lm/W respectively. The spin-coated device employing OCBzC exhibited a specific interaction at the surface of the film. Therefore, it reached a peak current efficiency of 4.57 cd/A and overperformed its control group lacking the TCTA layer. Moreover, TCTA OEP also presented a higher-quality image under external chip driving compared to its control group (Fig. S8c in Supporting information).

3.4.2. Solar cells

CMPs synthesized through electrochemical deposition can serve as effective HTL in solar cells. Its chemical stability makes it stand out as a promising option compared to materials like poly(3,4-ethylenedioxylenethiophene):poly(styrenesulfonate) (PEDOT:PSS), which have acidity issues. A pH-neutral CMP film containing carbazole group was synthesized through *in-situ* electrochemical deposition [141]. CMP films with an optimal thickness of 30 nm served as HTLs for ITO/CMP/PTB7-Th:PC_{71}BM/PFN/Al organic solar cells (Fig. S8d in Supporting information). It exhibited enhanced performance compared to PEDOT:PSS due to higher open-circuit voltage (V_{OC}) and short-circuit current (J_{SC}). This was attributed to a deeper HOMO level and modulation of the built-in potential. External quantum efficiency (EQE) measurements confirm the higher photocurrent. Such enhancement led to improved J_{SC}. PTB7-Th:PC_{71}BM solar cell equipped with CMP HTL performed better compared to that with PEDOT:PSS under optimal deposition conditions. Moreover, the hygroscopic and acidic nature of PEDOT:PSS often corroded ITO, which can accordingly reduce the chemical stability and efficiency of PEDOT-based devices and significantly shorten the practical lifespan of solar cells. Gu *et al*. reported a CMP *in-situ* synthesized through EP [38]. Later, the CMP film was integrated into the cell as anode interlayer and the final devices exhibited remarkable performance improvements. Optimized $LiClO_4$-doped CMP film achieved a full-around enhancement in power conversion efficiency (PCE), luminous efficiency, V_{OC}, J_{SC}, and fill factor (FF). These results prove that incorporating CMP films and doped CMP films could be excellent choices in advancing the electrochemical performance of organic electronic devices.

The same team prepared CMP films by EP using the precursor TPTCz. They polymerized a tetraphenylmethane core with peripheral carbazole groups and fabricated PSCs with the structure as shown in Fig. S8e (Supporting information) [142]. The performance of PSCs with undoped CMP films showed a PCE of 4.87 %, which significantly improved to 8.03 % with moderately doped CMP films. Specifically, PSCs with undoped CMP films exhibited a V_{OC} of 0.740 V, J_{SC} of 9.94 mA/cm^2, and FF of 66.2 %. In contrast, PSCs with moderately doped CMP films showed higher V_{OC} of 0.755 V

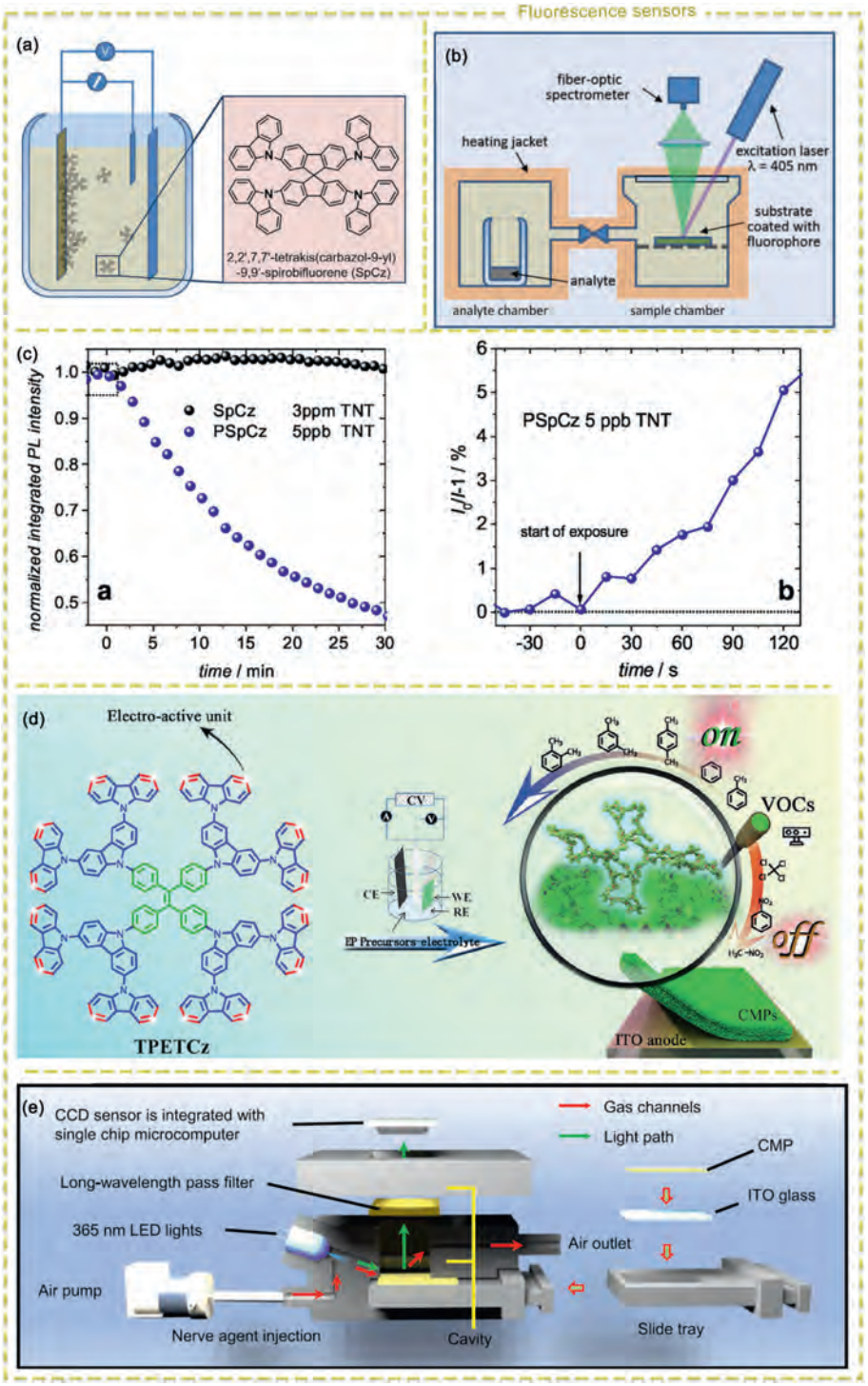


Fig. 4. (a) The principle behind electrochemical polymerization involves forming a microporous network, PSpCz, from a monomer solution of SpCz. Copied with permission [135]. Copyright 2016, Nature Publishing Group. (b) The setup for characterizing the photoluminescence of sensors. Copied with permission [135]. Copyright 2016, Nature Publishing Group. (c) A schematic comparison of the integrated photoluminescence intensity response between SpCz and PSpCz under different TNT exposure levels. Copied with permission [135]. Copyright 2016, Nature Publishing Group. (d) The molecular structure of TPETCz and the electrochemical polymerization process of CMP films. Copied with permission [40]. Copyright 2020, Wiley Publishing Group. (e) The schematic internal components of the portable detection system. Copied with permission [45]. Copyright 2022, Nature Publishing Group.

and J_{SC} of 16.76 mA/cm^2 with a slightly lower FF of 63.5 %. Doped CMP films not only improved both V_{OC} and J_{SC} but also overcame the typical trade-off between them in practical applications. Additionally, either doped CMP films or undoped CMP films demonstrated high FF values. It indicated sufficient contact on the interface between the active layer and CMP films. The efficiency of moderately doped PSCs was mainly due to higher J_{SC} compared to lightly doped ones (Fig. S8f in Supporting information). However, PSCs with a high level of doping exhibited lower efficiency due to uneven carrier concentration and such excessive dopant content led to the reduced carrier collection selectivity. As a result, the optimizing cathode led to efficient PSCs with a PCE of 8.42 %.

A year later, Gu *et al.* synthesized BTT-CMP and TTB-CMP using the same method (Fig. S8g in Supporting information) [143]. They constructed solar cells ITO/PEDOT:PSS/CMP:C_{60} film/LiF/Al and vacuum-deposited a 0.5 nm LiF layer and a 100 nm Al layer onto the BTT-CMP:C_{60} and TTB-CMP:C_{60} photoactive layers (Fig. S8h in Supporting information). Cells with BTT-CMP:C_{60} layers turned out achieving a superior PCE of 5.02 %. In comparison, cells with TTB-CMP:C_{60} layers exhibited a lower PCE of 2.55 %, 0.127 V more in V_{OC}, 5.14 mA/cm^2 more in J_{SC}, and 0.077 less in FF. These differences were due to variations in hole mobility and HOMO energy levels between the two CMP films.

3.4.3. Semiconductor

Compared to carbon materials, metal disulfides, nitride carbon, and graphene-like derivatives, organic semiconductors possess unique advantages, including low-temperature solution processability, lightweight, cost-effectiveness, high flexibility, controllable structure, and wide variety. Ranjeesh *et al.* synthesized a CMP by connecting a debranching carbazole acceptor benzene and pyrene containing acetylene groups through the Sonogashira-Hagihara coupling reaction (Fig. S9a in Supporting information) [144]. The calculated Tauc plots showed optical bandgaps of 1.76 and 1.58 eV for BI and PI, respectively, which indicated their excellent semiconductor properties (Figs. S9b and c in Supporting information). The activation reaction improved the filling of functional groups such as silanol on the substrate surface (Fig. S9d in Supporting information). Such enhancement improved the adhesion of 2D-CMP drop-cast films and increased the surface hydrophilicity of the thermal oxide substrate after oxygen plasma treatment. This is helpful to clean, activate, and modify the surface. Studies revealed that BI and PI materials exhibited negative Hall coefficients, consistent with electron-conducting characteristics. Hall effect measurements yielded carrier densities of approximately 5×10^{15} and 0.33×10^{15} cm^{-3} at room temperature for PI and BI-CMP films, respectively, which resulted in conductivity values of approximately 5.3 and 0.17 mS/cm [145,146]. From both structural and electronic perspectives, PI materials exhibited superior performance, which is advantageous for carrier transport and separation. This was attributed to their lower effective masses of electrons/holes along the π-columns direction. It confirmed the Hall effect measurement results and suggested that PI has more delocalized and mobile carriers than BI. The Hall effect measurement results and density functional theory (DFT) calculations-based mobility showed that PI and BI films not only exhibit excellent n-type semiconductor characteristics but also surpass previous CMP records in terms of carrier mobility and conductivity [145–147].

Despite the successful performance of these experiments, methods for fabricating films on conductive substrates, such as EP and oxidative coupling reactions, present significant challenges. These methods are generally suitable for small-area films but not for large-area carbon electronics [148–151]. To address this issue, Ju *et al.* fabricated a large-area patterned CMP film *via in situ* photopolymerization [132,152]. The preparation process of carbon nanofilms (CNFs) is demonstrated in Fig. S9e (Supporting information). Initially, carbazole monomers were spin-coated onto cleaned SiO_2/Si substrates, and carbazole was directly coupled using surface-confined polymerization. The obtained CMP films were then annealed under N_2 gas flow at different temperatures to convert them into CNFs. The size of CNFs was approximately 1 cm^2. By heating patterned CMP nanofilms, CNFs can be patterned into desired geometric shapes. To improve the photoresponsive performance of CNFs, carbon dots (CDs) were introduced by being sprayed on the surface of CNFs to form a CDs/CNFs heterostructure layer. Later, CDs/CNFs was used to construct a photodetector. It is worth noting that an enhanced photoinduced charge transfer phenomenon between CDs and CNF-750 was detected. Such enhanced charge transferring led to the enhanced photocurrent in the mixture under light condition. Furthermore, it also suggested that CDs play a key role in improving the device's photosensitivity.

3.5. Catalyst

3.5.1. Photocatalysts

CMP films possess intrinsic advantages for long-range charge delocalization and sufficient surface reactions due to their high porosity, film-like shape topological structure, and highly conjugated structural extensions. Narrow bandgap and efficient charge separation mechanism are key foundations for efficient photocatalytic hydrogen production material without the need for metal co-catalysts [153]. Wang *et al.* synthesized two CMP films that could be used as distinct semiconducting polymers for water splitting powered by visible light [41]. The band gaps of PTEPB and PTEB were 2.87 and 2.95 eV respectively, which strongly suggested that they were both promising candidates for visible-light photocatalysis. The average H_2 production rate for PTEPB was 218 μmol h^{-1} g^{-1}, while for PTEB, it was 102 μmol h^{-1} g^{-1}. XPS spectra of the catalytically terminated PTEPB and PTEB confirmed the absence of oxidized carbon atoms. It indicated the high stability of their conjugated 1,3-diyne structures. Computational results suggested two possible mechanics for the oxygen evolution reaction (OER) happened on PTEPB and PTEB photocatalysts: one was a single-site process involving the formation of *OOH and the other one was a dual-site process requiring the presence of two adjacent active sites to form *O*OH (Figs. S10a and b in Supporting information). In the hydrogen evolution reaction (HER), specific carbon atoms in PTEPB like carbon atom "7" served as active sites. This carbon atom showed the most favorable Gibbs free energy change. However, for PTEB, only carbon atom "3" served as an active site, since the reduction potential U_e provided by photogenerated electrons was small. These computational results unequivocally demonstrated that both PTEPB and PTEB were capable of catalyzing most water-splitting reactions. The OVS-Py-BT CMP synthesized by Kou *et al.* had a similar bandgap of 2.83 eV [154]. However, due to the two-branched structure of precursors, the obtained OVS-Py-BT CMP boasted a BET of 354 m^2/g. The average H_2 production rate for OVS-Py-BT was 1348 μmol h^{-1} g^{-1}, which is 6 times bigger than PTEPB (Fig. S10c in Supporting information). High surface area is important for catalysis, because it guarantees more active sites for reaction, which can accelerate the chemical reaction rate. The suface area of OVS-Py-BT is 4 times bigger than that of compared group. However, apart from using low-functionality precursors, the same group achieved a H_2 production rate of 77,935.10 μmol h^{-1} g^{-1} by constructing D-π-A structure [155]. The introduction of benzoin can promote the separation of photogenerated electrons and holes and facilitate electron transfer and the generation of H_2. Apart from introducing benzoin, introducing nanoparticles like bimetallic AuPd can increase the local temperature of aza-fused CMP nanosheets and achieve highly efficient catalysis under external light illumination without extra heating [156].

However, the photoreduction of CO_2 faces three main challenges: (i) The high C=O bond energy leads to a low product formation rate [157]; (ii) The multi-proton coupling and charge transfer processes result in poor selectivity of the reduction products [158]; (iii) The eight-electron transfer process for reducing CO_2 to CH_4 poses significant kinetic difficulties [159]. Increasing the π-conjugated system in CMPs can effectively extend the charge carrier migration distance and then modulate the exciton binding energy to promote intramolecular charge transfer and separation by reducing the exciton binding energy.

3.5.2. Electrocatalyst

The application of CMP films in electrocatalysis effectively addresses the challenge of catalyst recovery. Through EP, CMP films can be directly and securely deposited onto the electrode during synthesis. FeTCPP underwent EP in dichloromethane through potential cycling ranging from 0.4 V to 1.4 V *vs.* SCE at a scan rate of 0.2 V/s (Fig. S10d in Supporting information) [160]. The BET of PTEPB and PTEB reached 630 and 614 m^2/g. After incorporating FeTCPP into the carbazole film, the catalytic activity remains unchanged. This film not only served as an electrocatalyst but also the channel for the electron hopping. However, the structure of materials containing functionalized Fe-porphyrins was easily altered by CO_2 during the reduction process. Hod *et al.* encountered similar issues when electrodepositing iron porphyrins on electrodes for CO_2 electrolysis [161]. Fortunately, N-doping circumvents this problem nicely. Marco *et al.* delved into the oxygen reduction reaction (ORR) and investigated the reason for this phenomenon [71]. It was found out that N-doping glassy-carbon electrode exhibited higher positive potential than the bare one. The remarkable catalytic performance of TIPS-CMP showed comparable ORR performance to other catalysts without carbonization steps or mixing with different carbonaceous supports. The Koutecky-Levich plot of TIPS-CMP showed that the process of electron transfer in an oxygen reduction reaction (ORR) may be three-electron. This three-electron process may consist of two different mechanisms: A two-electron mechanism, where O_2 was reduced to hydrogen peroxide H_2O_2, and a four electron mechanism, where oxygen O_2 was reduced to water H_2O (Fig. S10e in Supporting information).

In the electrocatalytic conversion of CO_2, the use of suitable electrocatalysts can effectively lower the energy barrier and enhance reaction selectivity [158,162,163]. Studies have shown that combining metal phthalocyanines and their polymers with CNTs can significantly improve the efficiency and stability of CO_2 reduction to CO [164,165]. Wang *et al.*, by employing a Scholl coupling reaction *via* ionothermal method, copolymerized phthalocyanine and cobalt phthalocyanine around the surface of CNTs to synthesize a CNT@CMP(CoPc-H_2Pc) electrocatalyst with a specific surface area of 70 m^2/g (Fig. S10f in Supporting information) [166]. The nucleophilicity promotion of H_2Pc moiety on CoN_4 center led to a CO production current density of 15.2 mA/cm^2 from −0.6 V to −1.1 V *vs.* RHE. In a flow cell, this catalyst maintained an excellent 96 % Faradaic efficiency for CO conversion even when current densities exceeded 200 mA/cm^2.

4. Conclusions and perspective

CMP films have received quite attention due to their remarkable features above. The versatility of their synthesis and outstanding chemical and physical advantages have paved the way for their multiple applications across a spectrum of fields. Even though CMP films have found their place in various fields, there are still some challenges hindering their further advancement.

(i) Organic electronics products are often challenged by precise doping control and management of surface morphology. Therefore, controlling the doping level in CMP films is vital to improving device performance. The efficiency of the device, especially for OLEDs, is directly affected by the doping level.

(ii) When it comes to semiconductors, the inherently low electrical conductivity of CMP films is a significant challenge. For batteries, CMPs can significantly enhance capacity through π-π stacking and hydrogen bonding. However, CMP films suffer from limited active sites, structural instability, poor cycling stability, and inadequate conductivity/ion transport rates, ultimately hindering their practical applications [109].

(iii) The thickness of the CMP film is the key factor to prevent current leakage. The precise control over CMP films' thickness is important to achieve the desired structure and surface properties. Fortunately, EP provides a possible answer. However, during the EP process, highly concentrated monomer solutions are required. Moreover, the depletion of monomer concentration during the EP process might lead to the generation of oxides and cause the deterioration and aging of CMP films.

(iv) Their mechanical and chemical stability restricts the long-term use of certain CMP films in applications such as chemical capture and separation, electrocatalysts, and sensors. Moreover, it is difficult to maintain a consistent pore size to permeate ions selectively.

(v) Last but not least, scalability is another significant obstacle in the commercialization of CMP films. The challenge of achieving large-scale production is not limited to traditional synthesis methods. The prevalent EP method also suffers from the same problems and new fabrication technologies are still urgently needed.

The future of CMP films is poised for significant advances across various applications once they overcome existing challenges and harness their full potential. The crucial issue among these advancements is the tuning of pore sizes within CMP films. This capability holds the potential to transform drug delivery, chiral catalysis, ion storage, and pollutant separation by allowing for precise control over molecular interactions. Similarly, alerting the composition of CMP building blocks could adjust the absorption wavelength and vastly improve their efficiency in energy conversion applications such as photocatalytic hydrolysis and OSCs. The development of intelligent portable devices that use CMP films underscores their potential to foster technological progress toward a sustainable and health-conscious society. However, there is still a long way to go when it comes to achieving outstanding durability and mechanical integrity of CMP films through designing and optimizing the molecular structures. Traditional CMP materials require harsh synthesis conditions, which makes film formation full of challenges. Although academic research has made progress in CMP film preparation methods like interfacial polymerization and electrochemical synthesis. These approaches often face scalability issues. Even though electropolymerization has been proposed, they demand high precision in equipment and reaction control and resulting in elevated industrialization costs. The exploration of transforming CMP powders to CMP films is essential for ensuring scalability, safety, and cost efficiency, which are pivotal for the commercialization of CMP-based technologies. While CMP films exhibit promising properties for diverse applications, such as enhanced electrochemical performance through optimized molecular design, flexibility for wearable electronics, and environmentally friendly synthesis methods, their full integration into practical devices requires addressing critical challenges. Future development should focus on advancing scalable production processes, expanding applications to energy storage systems like solid-state batteries, and using their unique microporous structure to tackle issues like polysulfide shuttling. Additionally, integrating CMP films with smart-responsive materials could enable adaptive functionalities. To realize their potential, collaborative efforts in fundamental research and industrial R&D are imperative to overcome technical barriers and bridge the gap between laboratory innovation and market-ready solutions.

Declaration of competing interest

The authors declare that they have no known competing financial interests or personal relationships that could have appeared to influence the work reported in this paper.

CRediT authorship contribution statement

Wang Wang: Writing – original draft. **Miao Feng:** Writing – original draft. **Shuqi Zou:** Formal analysis. **Chunxia Chen:** Funding acquisition. **Jinsong Peng:** Funding acquisition. **Xiaobai Li:** Writing – review & editing. **Shitong Zhang:** Writing – review & editing. **Xin Ai:** Writing – review & editing, Conceptualization. **Hongwei Ma:** Writing – review & editing, Funding acquisition, Conceptualization.

Acknowledgments

This work was financially supported by National Key R&D Program of China (No. 2023YFF1304903), National Natural Science Foundation of China (Nos. 22374017, 62205052), Fundamental Research Funds for the Central Universities (No. 2572023CT12), the Natural Science Foundation of Heilongjiang Province (No. YQ2024B003).

Supplementary materials

Supplementary material associated with this article can be found, in the online version, at doi:10.1016/j.cclet.2025.111611.

References

[1] P. Arab, M.G. Rabbani, A.K. Sekizkardes, et al., Chem. Mater. 26 (2014) 1385–1392.
[2] B. Li, Y. Zhang, R. Krishna, et al., J. Am. Chem. Soc. 136 (2014) 8654–8660.
[3] X. Zhu, C. Tian, S.M. Mahurin, et al., J. Am. Chem. Soc. 134 (2012) 10478–10484.
[4] X. Zhu, C. Tian, G.M. Veith, et al., J. Am. Chem. Soc. 138 (2016) 11497–11500.
[5] Z.J. Wang, S. Ghasimi, K. Landfester, K.A. Zhang, Chem. Mater. 27 (2015) 1921–1924.
[6] Y.L. Wong, J. Tobin, Z. Xu, F. Vilela, J. Mater. Chem. A 4 (2016) 18677–18686.
[7] J. Byun, K.A. Zhang, Mater. Horizons 7 (2020) 15–31.
[8] S. Luo, Z. Zeng, G. Zeng, et al., J. Mater. Chem. A 8 (2020) 6434–6470.
[9] Y. Kou, Y. Xu, Z. Guo, D. Jiang, Angew. Chem. 50 (2011) 8753–8757.
[10] A.M. Khattak, H. Sin, Z.A. Ghazi, et al., J. Mater. Chem. A 6 (2018) 18827–18832.
[11] K. Amin, N. Ashraf, L. Mao, C.F. Faul, Z. Wei, Nano Energy 85 (2021) 105958.
[12] B. Bonillo, R.S. Sprick, A. Cooper, Chem. Mater. 28 (2016) 3469–3480.
[13] C. Yang, B.C. Ma, L. Zhang, et al., Angew. Chem. Int. Ed. 55 (2016) 9202–9206.
[14] Z. Li, H. Li, H. Xia, et al., Chemistry 21 (2015) 17355–17362.
[15] F. Mao, P.F. Liu, P. Yang, J. Gu, H.G. Yang, Chem. Commun. 56 (2020) 7495–7498.
[16] A. Rengaraj, P. Puthiaraj, Y. Haldorai, et al., ACS Appl. Mater. Interfaces 8 (2016) 8947–8955.
[17] J. Hynek, J. Rathouský, J. Demel, K. Lang, RSC Adv. 6 (2016) 44279–44287.
[18] Y. Liao, Z. Cheng, W. Zuo, A. Thomas, C.F.J. Faul, ACS Appl. Mater. Interfaces 9 (2017) 38390–38400.
[19] Y.B. Zhou, Z.P. Zhan, Chem. Asian J. 13 (2018) 9–19.
[20] A. Singh, S. Roy, C. Das, D. Samanta, T.K. Maji, Chem. Commun. 54 (2018) 4465–4468.
[21] W. Zhao, G. Wang, Physica D 399 (2019) 42–50.
[22] S. Roy, A. Bandyopadhyay, M. Das, et al., J. Mater. Chem. A 6 (2018) 5587–5591.
[23] X. Tan, S. Robijns, R. Thür, Q. Ke, et al., Science 378 (2022) 1189–1194.
[24] H. Sha, J. Cui, J. Li, et al., Sci. Adv. 9 (2023) eadf1151.
[25] A. Carné-Sánchez, G.A. Craig, P. Larpent, T. Hirose, et al., Nat. Commun. 9 (2018) 2506.
[26] J. Chen, M. Longo, A. Fuoco, et al., Angew. Chem. Int. Ed. 62 (2023) e202215250.
[27] S. Ye, N. Hosono, T. Uemura, Adv. Funct. Mater. 34 (2024) 2312265.
[28] L. Zhang, B. Luo, K. Fu, et al., Adv. Sci. 10 (2023) e2304187.
[29] S. Lin, C.S. Diercks, Y.B. Zhang, et al., Science 349 (2015) 1208–1213.
[30] Z. Teng, Z. Zhang, H. Yang, et al., Sci. Adv. 10 (2024) eadl5432.
[31] Q. Zhang, S. Dong, P. Shao, et al., Science 378 (2022) 181–186.
[32] J.X. Jiang, F. Su, A. Trewin, et al., Angew. Chem. Int. Ed. 46 (2007) 8574–8578.
[33] N.B. Mckeown, S. Makhseed, P.M. Budd, Chem. Commun. 23 (2002) 2780–2781.
[34] A.I. Cooper, Adv. Mater. 21 (2009) 1291–1295.
[35] E.Q. Jin, M. Asada, Q. Xu, et al., Science 357 (2017) 673–676.
[36] K. Zhang, D. Kopetzki, P.H. Seeberger, M. Antonietti, F. Vilela, Angew. Chem. Int. Ed. 52 (2013) 1432–1436.
[37] L. Chen, Y. Honsho, S. Seki, D. Jiang, J. Am. Chem. Soc. 132 (2010) 6742–6748.
[38] C. Gu, Y. Chen, Z. Zhang, et al., Adv. Mater. 25 (2013) 3443–3448.
[39] Y. Jia, S. Chen, X. Meng, et al., Small 19 (2023) 2303919.
[40] H. Liu, Y. Wang, W. Mo, et al., Adv. Funct. Mater. 30 (2020) 1910275.
[41] L. Wang, Y. Wan, Y. Ding, et al., Adv. Mater. 29 (2017) 1702428.
[42] J.X. Jiang, A. Trewin, D.J. Adams, A.I. Cooper, Chem. Sci. 2 (2011) 1777.
[43] F. Ren, F. Wang, Y. Pan, et al., Macromol. Mater. Eng. 303 (2018) 1700619.
[44] C. Gu, N. Huang, J. Gao, et al., Angew. Chem. Int. Ed. 53 (2014) 4850–4855.
[45] W. Mo, Z. Zhu, F. Kong, et al., Nat. Commun. 13 (2022) 5189.
[46] J. Tan, J.X. Wan, J. Guo, C.C. Wang, Chem. Commun. 51 (2015) 17394–17397.
[47] S.H. Ryu, D.H. Lee, Y.J. Ko, et al., Macromol. Chem. Phys. 220 (2019) 1900157.
[48] Z.Y. Zhou, D.B. Shinde, D. Guo, et al., Adv. Funct. Mater. 32 (2022) 2108672.
[49] J. Long, Y.X. Liu, Z.F. Huang, et al., Chem. Eur. J. 30 (2024) e202304268.
[50] Z.Y. Li, J.Z. Song, X.Y. Gao, et al., Chin. Chem. Lett. 36 (2025) 110073.
[51] Y. Xu, L. Chen, Z. Guo, A. Nagai, D. Jiang, J. Am. Chem. Soc. 133 (2011) 17622–17625.
[52] B. Liang, H. Wang, X. Shi, et al., Nat. Chem. 10 (2018) 961–967.
[53] T. Chen, W. Zhang, B. Li, et al., ACS Appl. Mater. Interfaces 12 (2020) 56385–56392.
[54] T. Banerjee, K. Gottschling, G. Savasci, C. Ochsenfeld, B.V. Lotsch, ACS Energy Lett. 3 (2018) 400–409.
[55] Y. Bai, L. Wilbraham, B.J. Slater, et al., J. Am. Chem. Soc. 141 (2019) 9063–9071.
[56] Y. Qin, S. Jha, C.M. Hu, et al., J. Colloid Interface Sci. 675 (2024) 1091–1099.
[57] X.Z. Yang, C.M. Hu, Y.M. Chen, et al., J. Energy Storage 104 (2024) 114509.
[58] J. Schmidt, M. Werner, A. Thomas, Macromolecules 42 (2009) 4426–4429.
[59] S.Y. Liu, T.S. Yan, Q.X. Wu, Z. Xu, J. Han, Chin. Chem. Lett. 33 (2022) 239–242.
[60] J. Liu, H. Li, J. Wang, et al., Adv. Energy Mater. 11 (2021) 2101926.
[61] D. Ruiz-Martinez, R. Grieco, M. Liras, N. Patil, R. Marcilla, Adv. Energy Mater. 14 (2024) 2400857.
[62] L. Zhong, Z. Fang, C. Shu, et al., Angew. Chem. Int. Ed. 60 (2021) 10164–10171.
[63] W. Lyu, W. Zhang, H. Liu, et al., Chem. Mater. 32 (2020) 8276–8285.
[64] J. Chen, W. Yan, E.J. Townsend, et al., Angew. Chem. Int. Ed. 58 (2019) 11715–11719.
[65] A. Palma-Cando, U. Scherf, Macromol. Chem. Phys. 217 (2016) 827–841.
[66] D. Zhou, K. Zhang, S. Zou, X. Li, H. Ma, J. Mater. Chem. A 12 (2024) 17021–17053.
[67] M.G. Mohamed, A.F.M. EL-Mahdy, M.G. Kotp, S.W. Kuo, Mater. Adv. 3 (2022) 707–733.
[68] M.G. Mohamed, E.C. Atayde Jr., B.M. Matsagar, et al., J. Taiwan Inst. Chem. Eng. 112 (2020) 180–192.
[69] K. Yuan, P. Guo-Wang, T. Hu, et al., Chem. Mater. 27 (2015) 7403–7411.
[70] J. Stille, E. Mainen, Macromolecules 1 (1968) 36–42.
[71] A.B. Marco, D. Cortizo-Lacalle, I. Perez-Miqueo, et al., Angew. Chem. Int. Ed. 56 (2017) 6946–6951.
[72] T. Yamamoto, Y. Hayashi, A. Yamamoto, Bull. Chem. Soc. Jpn. 51 (1978) 2091–2097.
[73] M. Trunk, A. Herrmann, H. Bildirir, A. Yassin, J. Schmidt, A. Thomas, Chem. Eur. J. 22 (2016) 7179–7183.
[74] S. Thorand, N. Krause, J. Org. Chem. 63 (1998) 8551–8553.
[75] C. Yan, N. Meng, W. Lyu, et al., Carbon 176 (2021) 178–187.
[76] J. Zhan, A.F. El-Mahdy, Chem. Eng. J. 473 (2023) 145124.
[77] J.H. Lee, D.J. Won, H.W. Kim, H.J. Park, J. Food. Eng. 256 (2019) 1–8.
[78] D. Wang, L. Li, W. Yang, et al., RSC Adv. 4 (2014) 59877–59884.
[79] C. Xu, N. Hedin, J. Mater. Chem. A: Mater. 1 (2013) 3406–3414.
[80] R. Dawson, A.I. Cooper, D.J. Adams, Prog. Polym. Sci. 37 (2012) 530–563.
[81] P. Lindemann, M. Tsotsalas, S. Shishatskiy, et al., Chem. Mater. 26 (2014) 7189–7193.
[82] A. Prasad, G. Fotou, S.T. Li, J. Mater. Res. 28 (2013) 2380–2393.
[83] Y. Xu, S. Jin, H. Xu, A. Nagai, D. Jiang, Chem. Soc. Rev. 42 (2013) 8012–8031.
[84] X. He, H. Sin, B. Liang, et al., Adv. Funct. Mater. 29 (2019) 1900134.
[85] E.J. Dell, L.M. Campos, J. Mater. Chem. 22 (2012) 12945–12952.
[86] E. Amir, S. Rozen, Angew. Chem. Int. Ed. 44 (2005) 7374–7378.
[87] Y. Suzuki, T. Okamoto, A. Wakamiya, S. Yamaguchi, Org. Lett. 10 (2008) 3393–3396.
[88] D. Guo, X. Li, W. Wahyudi, et al., ACS Nano 14 (2020) 17163–17173.
[89] R. Hardian, K.A. Miller, L. Cseri, et al., Chem. Eng. J. 452 (2023) 139457.
[90] Q. Su, Y. Wang, J. Chen, D. Zhao, H. Long, M. Li, Chem. Eng. J. 457 (2023) 141130.
[91] H.B. Park, J. Kamcev, L.M. Robeson, M. Elimelech, B.D. Freeman, Science 356 (2017) eaab0530.
[92] M. Zhang, X. Jing, S. Zhao, et al., Angew. Chem. Int. Ed. 58 (2019) 8768–8772.
[93] Z. Zhou, D. Guo, D.B. Shinde, et al., ACS Nano 15 (2021) 11970–11980.
[94] H.B. Park, C.H. Jung, Y.M. Lee, et al., Science 318 (2007) 254–258.
[95] J. Yang, P. Liu, X. He, et al., Angew. Chem. Int. Ed. 59 (2020) 6244–6248.
[96] Z. Zhou, D.B. Shinde, D. Guo, et al., Adv. Funct. Mater. 32 (2022) 2108672.
[97] X. Guan, Y.J. Zhao, H.J. Pei, et al., Chem. Eng. J. 473 (2023) 144733.
[98] J.M. Dawlaty, S. Shivaraman, M. Chandrashekhar, F. Rana, M.G. Spencer, Appl. Phys. Lett. 92 (2008) 042116.
[99] Y. Tian, G. Li, Y. Zhang, et al., Adv. Mater. 32 (2020) 1904876.
[100] L. Sun, X. Meng, J. Zhang, et al., J. Power Sources 575 (2023) 233173.
[101] S.Y. Yu, J. Mahmood, H.J. Noh, et al., Angew. Chem. Int. Ed. 57 (2018) 8438–8442.
[102] X.J. Zhao, S.Y. Qin, F. Wu, et al., Chin. Chem. Lett. 36 (2025) 110246.
[103] D. Guo, X. Li, F. Ming, et al., Nano Energy 73 (2020) 104769.
[104] A. Miura, N.C. Rosero-Navarro, A. Sakuda, K. Tadanaga, et al., Nat. Rev. Chem. 3 (2019) 189–198.
[105] K. Zhang, W. Liu, Y. Gao, et al., Adv. Mater. 33 (2021) 2006323.
[106] Y. Hu, W. Tang, Q. Yu, C. Yang, C. Fan, ACS Appl. Mater. Interfaces 11 (2019) 32987–32993.

[107] W. Deng, W. Shi, P. Li, et al., Energy Storage Mater. 46 (2022) 535–541.
[108] Z. Yu, L. Huang, Y. Wang, et al., Energy Storage Mater. 66 (2024) 103220.
[109] C.M. Hu, Y.M. Chen, Z.Y. Song, et al., J. Mater. Chem. A 12 (2024) 12818–12825.
[110] A.A. Khan, I. Muhammad, R. Ahmad, et al., Comput. Mater. Sci. 214 (2022) 111757.
[111] N. An, J. Xin, W.L. Li, et al., Appl. Surf. Sci. 599 (2022) 153881.
[112] J. Aslam, M.A. Waseem, W.W. Sun, Y. Wang, Chem. Eng. J. 500 (2024) 156578.
[113] Y.C. Jia, W.B. Gong, X.Y. Fan, et al., Chem. Eng. J. 444 (2022) 136546.
[114] H. Zhang, Y. Zhang, C. Gu, Y. Ma, Adv. Energy Mater. (2015) 1402175.
[115] H. Macit, S. Sen, M. Sacak, J. Appl. Polym. Sci. 96 (2005) 894–898.
[116] V. Raj, D. Madheswari, M. Mubarak Ali, J. Appl. Polym. Sci. 116 (2010) 147–154.
[117] M.G. Mohamed, C.C. Chen, M. Ibrahim, et al., JACS Au 4 (2024) 3593–3605.
[118] P. Fiordiponti, G. Pistoia, Electrochim. Acta 34 (1989) 215–221.
[119] Y. Dai, W. Li, Z. Chen, et al., J. Mater. Chem. A 7 (2019) 16397–16405.
[120] K. Yuan, X. Zhuang, H. Fu, et al., Angew. Chem. Int. Ed. 55 (2016) 6858–6863.
[121] L. Teng, J. Duan, H. Liu, et al., J. Mater. Chem. A: Mater. 12 (2024) 12423–12434.
[122] M.M. Samy, M.G. Mohamed, S.U. Sharma, et al., J. Taiwan Inst. Chem. Eng. 158 (2024) 104750.
[123] S.V. Chaganti, S.U. Sharna, M. Ibrahim, et al., J. Power Sources 627 (2025) 235848.
[124] A. Basit, M.G. Mohamed, S.U. Sharma, et al., ACS Appl. Polym. Mater. 6 (2024) 12247–12260.
[125] A. Palma-Cando, E. Preis, U. Scherf, Macromolecules 49 (2016) 8041–8047.
[126] S. Bai, Q. Hu, Q. Zeng, M. Wang, L. Wang, ACS Appl. Mater. Interfaces 10 (2018) 11319–11327.
[127] W. Song, J. Sun, Q. Wang, et al., Mater. Horiz. 11 (2024) 1023–1031.
[128] G. Gou, L. Fang, M. Wang, et al., Adv. Opt. Mater. 11 (2023) 2300489.
[129] J. Song, H. Lu, M. Liu, et al., Small 20 (2024) 2308595.
[130] C. Cho, P. Kang, A. Taqieddin, et al., Nat. Electron. 4 (2021) 126–133.
[131] W. Xiong, Y. Gong, Y. Che, J. Zhao, Anal. Chem. 91 (2019) 1711–1714.
[132] L. Chen, D. Liu, J. Peng, Q. Du, H. He, Coord. Chem. Rev. 404 (2020) 213113.
[133] A.J. Lopez, D. Ruiz-Molina, K. Landfester, M.B. Bannwarth, C. Roscini, Adv. Funct. Mater. 28 (2018) 1801492.
[134] S. Jiang, L.C. Meng, W.Y. Ma, et al., Chin. Chem. Lett. 32 (2021) 1037–1040.
[135] A. Räupke, A. Palma-Cando, E. Shkura, et al., Sci. Rep. 6 (2016) 29118.
[136] L. Zhou, Y. Peng, Y. Hu, G. Li, J. Anal. Test. 1 (2017) 5.
[137] J. Luo, Z. Xie, J.W. Lam, et al., Chem. Commun. (2001) 1740–1741.
[138] M. Gross, D.C. Müller, H.G. Nothofer, et al., Nature 405 (2000) 661–665.
[139] A. Baba, K. Onishi, W. Knoll, R.C. Advincula, J. Phys. Chem. B 108 (2004) 18949–18955.
[140] Y. Liang, C. Liu, M. Zhao, et al., ACS Appl. Mater. Interfaces 12 (2020) 20714–20721.
[141] S. Yang, C. Yang, X. Zhang, et al., J. Mater. Chem. C 6 (2018) 9044–9048.
[142] C. Gu, Y. Chen, Z. Zhang, et al., Adv. Energy Mater. 8 (2014) 1301771.
[143] C. Gu, N. Huang, Y. Chen, et al., Angew. Chem. Int. Ed. 54 (2015) 13594–13598.
[144] K.C. Ranjeesh, A. Rezk, J.I. Martinez, S. Gaber, et al., Adv. Sci. 10 (2023) 2303562.
[145] H.J. Noh, S. Chung, M.S. Okyay, et al., Chem 8 (2022) 3130–3144.
[146] M. Souto, D.F. Perepichka, J. Mater. Chem. C 9 (2021) 10668–10676.
[147] M. Wang, M. Ballabio, M. Wang, et al., J. Am. Chem. Soc. 141 (2019) 16810–16816.
[148] Y. Liu, Y. Wei, M. Liu, et al., Angew. Chem. Int. Ed. 60 (2021) 2887–2891.
[149] W. Yao, J. Zhang, J. Ji, et al., Adv. Mater. 34 (2022) 2108608.
[150] J. Tang, Z. Liang, H. Qin, et al., Angew. Chem. Int. Ed. 62 (2023) e202214449.
[151] R. Chen, L. Zhang, Y. Zhou, et al., Giant 8 (2021) 100072.
[152] S. Ju, Y. Ding, Y. Yin, et al., RSC Adv. 9 (2019) 17399–17404.
[153] M.M. Samy, I.M.A. Mekhemer, M.G. Mohamed, et al., Chem. Eng. J. 446 (2022) 137158.
[154] M.G. Mohamed, M.H. Elsayed, A.E. Hassan, et al., ACS Appl. Polym. Mater. 6 (2024) 5945–5956.
[155] I.M.A. Mekhemer, A.M. Elewa, M.M. Elsenety, et al., Chem. Eng. J. 497 (2024) 154280.
[156] Y.N. Li, L. Wang, J.X. Low, et al., Chin. Chem. Lett. 31 (2020) 231–234.
[157] F. Wang, T. Hou, X. Zhao, et al., Adv. Mater. 33 (2021) 2102690.
[158] Y. Shi, J. Li, C. Mao, et al., Nat. Commun. 12 (2021) 5923.
[159] H. Rao, L.C. Schmidt, J. Bonin, M. Robert, Nature 548 (2017) 74–77.
[160] X.M. Hu, Z. Salmi, M. Lillethorup, et al., Chem. Commun. 52 (2016) 5864–5867.
[161] I. Hod, M.D. Sampson, P. Deria, et al., ACS Catal. 5 (2015) 6302–6309.
[162] X. Zhang, H. Liu, P. An, et al., Sci. Adv. 6 (2020) eaaz4824.
[163] O.S. Bushuyev, P. De Luna, C.T. Dinh, et al., Joule 2 (2018) 825–832.
[164] X. Zhuang, F. Zhang, D. Wu, et al., Angew. Chem. Int. Ed. 52 (2013) 9668–9672.
[165] C. Lu, J. Yang, S. Wei, et al., Adv. Funct. Mater. 29 (2019) 1806884.
[166] R. Wang, X. Wang, W. Weng, et al., Angew. Chem. Int. Ed. 61 (2022) e202115503.